McNulty, J. A. et al. (2019) An electronically driven improper ferroelectric: tungsten bronzes as microstructural analogues for the hexagonal manganites. *Advanced Materials*, 31(40), 1903620

There may be differences between this version and the published version. You are advised to consult the publisher's version if you wish to cite from it.

This is the peer reviewed version of the following article: McNulty, J. A. et al. (2019) An electronically driven improper ferroelectric: tungsten bronzes as microstructural analogues for the hexagonal manganites. *Advanced Materials*, 31(40), 1903620, which has been published in final form at http://dx.doi.org/10.1002/adma.201903620

http://eprints.gla.ac.uk/191703/

Deposited on: 2 August 2019

An Electronically Driven Improper Ferroelectric: Tungsten Bronzes as Microstructural Analogues for the Hexagonal Manganites

Jason A. McNulty[1], T. Thao Tran[2], P. Shiv Halasyamani[2], Shane J. McCartan[3], Ian MacLaren[3], Alexandra S. Gibbs[4], Felicia J. Y. Lim[5,6], Patrick W. Turner[5], J. Marty Gregg[5], Philip Lightfoot[1], Finlay D. Morrison[1,*].

[1]EaStCHEM School of Chemistry, University of St Andrews, St Andrews KY16 9ST, UK.
[2]Department of Chemistry, University of Houston, 3585 Cullen Blvd, 112 Fleming Building, Houston, TX 77204-5003, USA.
[3]School of Physics and Astronomy, University of Glasgow, Glasgow G12 8QQ, UK.
[4]ISIS Facility, Rutherford Appleton Laboratory, Chilton, Didcot, OX11 0QX, UK.
[5]School of Mathematics and Physics, Queen's University Belfast, University Rd., Belfast BT7 1NN, UK.
[6]Department of Mechanical Engineering, University of Sheffield, Sheffield S3 7QB, UK.

Abstract

Since the observation that the properties of ferroic domain walls (DWs) can differ significantly from the bulk materials in which they are formed, it has been realised that domain wall engineering offers exciting new opportunities for nano-electronics and nano-device architectures. We report a novel improper ferroelectric, $CsNbW_2O_9$, with the hexagonal tungsten bronze structure. Powder neutron diffraction and symmetry mode analysis indicate that the improper transition ($T_C \sim 1100$ K) involves unit cell tripling, reminiscent of the hexagonal rare earth manganites. However in contrast to the manganites the symmetry breaking in $CsNbW_2O_9$ is electronically driven (*i.e.,* purely displacive) *via* the second order Jahn-Teller effect in contrast to the geometrically driven tilt mechanism of the manganites. Nevertheless $CsNbW_2O_9$ displays the same kinds of domain microstructure as those found in the manganites, such as characteristic six-domain 'cloverleaf' vertices and DW sections with polar discontinuities. The discovery of a completely new material system, with domain patterns already known to generate interesting functionality in the manganites, is important for the emerging field of DW nanoelectronics.

Emergent phenomena at interfaces are increasingly offering new functionality in materials[1]: for example, 2D-electron gas (2DEG) behaviour at insulator-insulator interfaces (e.g. LaAlO$_3$/SrTiO$_3$[2]) or superconductivity in WO$_{3-\delta}$ twin walls[3]. More recently, demonstration of electrical properties at ferroelectric domain walls (DWs) that differ significantly from bulk has generated great excitement; unlike in the established 2DEG systems, the existence and position of DWs can be manipulated, *i.e.*, 'injected', displaced and 'annihilated' by external stimuli (such as electric fields). The aspiration is that these 2D-'sheet'-materials could therefore be exploited in new forms of agile nano-electronics[4]. Emergent electrical properties of DWs include enhanced or diminished electrical conductivity (both *ac* and *dc*) in a wide range of materials including BiFeO$_3$,[5, 6] BaTiO$_3$,[7, 8] LiNbO$_3$,[9] PZT[10], KTP[11], copper-chloride boracites[12] and members of the rare earth manganites (*R*MnO$_3$, *R* = Y, Er, Ho)[13-17]. The ambition to exploit DWs with different functionality for nano-electronics, however, stretches beyond simply reconfigurable circuitry which relies on DW conduction to direct current. The functional properties of DWs have also been demonstrated to include more complex behaviour such as rectification[15] and have already been utilized for nano-electronic devices including diodes[11], tunnel junctions[8] and non-volatile memories[6]. The electrical behaviour of DWs has been shown to be highly dependent on the nature of the discontinuity in the polarisation at the ferroelectric DW[18]: head-to-head, or tail-to-tail polarisation results in a wall with bound charge. In proper ferroelectrics, which have polarization as the order parameter, the domain configuration forms in order to minimize the electrostatic energy and depolarisation field (and in non-uniaxial systems to relieve mechanical strain); charged domains walls in proper ferroelectrics are therefore not favoured under normal conditions. In improper ferroelectrics, however, the polarisation is secondary to the, often purely structural, primary distortion mode which breaks the crystal symmetry at the Curie temperature, T_C. As a result, the ferroelectric phase is not the maximal polar subgroup of the space group of the non-polar, paraelectric phase[19]. Consequently, the ferroelectric domain structure of improper ferroelectrics is determined by the (non-polar) symmetry-breaking mode as the order parameter, rather than by polarisation.

The improper ferroelectric[20] rare earth manganites, *R*MnO$_3$ (R^{3+} = Dy, Ho, Er, Tm, Yb, Lu, Y, and Sc), in particular have generated widespread interest as the geometrically driven improper nature of ferroelectricity results in striking six-domain 'cloverleaf' vertices linked by labyrinthine (meandering) DWs with wide-ranging functionalities[13, 15-17]. Specifically the domain microstructure involves interlocking of (structural) antiphase and ferroelectric

boundaries[21] to produce the labyrinthine domain structures with six-domain vertices rather than conventional stripe or "tweed" patterns. In these complex domain structures the domain wall alignment meanders relative to the polarisation direction and in $ErMnO_3$ the DW conductivity has been shown to vary according to this alignment[13]. As the domain structure in the manganites is determined by the underlying topology of the crystal system this provides a fertile playground uniting topology and physical properties of materials as proposed by Kosterlitz[22]. This is typified by the geometrically driven mechanism for improper ferroelectricity observed in the hexagonal rare earth manganites and which was first proposed for $YMnO_3$[23] and was later confirmed experimentally[24]. In $YMnO_3$, symmetry breaking is geometrically driven by the small R-cation and involves tilting of the MnO_5 polyhedra; the underlying symmetry during this transition into the polar phase generates six-domain vertices ($\Delta\Phi = \pi/3$)[25, 26] commonly referred to as a "cloverleaf" domain structure. In addition to the complex domain structures, the mechanism which produces these topologically-protected vertices has also been used as a model system to mimic the formation of cosmic strings in the universe during the continuous (U1) symmetry breaking transition on cooling immediately after the big bang[27]. Here we present an alternative improper ferroelectric, $CsNbW_2O_9$, from an entirely different structural family (the hexagonal tungsten bronzes) which, despite being driven by an electronic distortion, also forms topologically protected six-domain vertices and a similar labyrinthine domain structure to that observed in the hexagonal manganites.

The hexagonal tungsten bronzes (HTBs) are derived from the hexagonal polymorph of tungsten trioxide (h-WO_3) which can be formed using low temperature synthetic routes[28], or by intercalation of large group 1 metals such as K^+, Rb^+ and Cs^+, to form A_xWO_3 $0.15 \leq x \leq 0.33$[29]. The compositional variability offered by the bronzes *via* such cation inter-/de-intercalation is well known and can be electrochemically driven due to the redox behaviour of the tungsten: $A_xW^V_xW^{VI}_{1-x}O_3$; these materials often exhibit metallic behaviour and are conducive to superconductivity[30]. It is possible to suppress electrical conductivity by replacement of W^{5+} (d^1) with d^0 cations and a wide range of compositions $A_yB_xW_{3-x}O_9$ with A = K^+, Rb^+, Cs^+, Tl^+ and B = Zn^{2+}, Sc^{3+}, Ti^{4+}, Zr^{4+}, Nb^{5+}, Ta^{5+} *etc.,* have been studied (see the comprehensive review by Isupov[31]). Although a number of these have been reported as ferroelectric[31], few studies have included physical property measurements in support of these claims, with the exception of the most recent studies of ABW_2O_9 with A = K^+, Rb^+ and B = Nb^{5+}, Ta^{5+} by Chang *et al.*,[32] and the underlying mechanisms of symmetry-breaking

have not been explored in detail. In addition, improper ferroelectricity has not previously been reported in this structural family.

Here we report the composition $CsNbW_2O_9$, which corresponds to full occupation of the hexagonal channels (A-sites) and where W^{5+} has been replaced by a $3d^0$ Nb^{5+} cation to mitigate against unwanted electrical conductivity. Variable temperature powder x-ray (PXRD) and neutron (PND) diffraction was used to follow the structural evolution of this material as a function of temperature, Figure 1. Full structural details can be found in the Supporting Information S1. At high temperature, the material adopts the high symmetry (*P6/mmm*) parent HTB aristotype with $a_{HTB} \approx 7.41$ Å and $c_{HTB} \approx 3.95$ Å, Figure 1a. Note that the "stoichiometric" material $CsNbW_2O_9$ contains a minor amount of the defect pyrochlore, $CsNbWO_6$. However this can be avoided by reducing the A-site occupancy and balancing the Nb-content accordingly: $Cs_{0.9}Nb_{0.9}W_{2.1}O_9$ is single phase HTB and exhibits the same structural behaviour as $CsNbW_2O_9$ (see Supporting Information S2). On cooling, an additional reflection, associated with scattering at the *K*-point (wavevector $\boldsymbol{k} = 1/3, 1/3, 0$) of the hexagonal parent Brillouin zone is observed by both PXRD and PND below 1100 K, Figure. 1b, indicating unit cell tripling ($a \approx 12.8$ Å $= \sqrt{3}a_{HTB}$). Below 350 K further additional reflections due to scattering at the *A*-point ($\boldsymbol{k} = 0, 0, ½$) indicate *c*-axis doubling ($c \approx 7.9$ Å $= 2c_{HTB}$), Figure 1c; these are only observable in the PND, not PXRD, data implying that this doubling is associated with the oxygen positions and subtle octahedral tilting, due to the relative insensitivity of PXRD to light atom positions. This *c*-axis doubled hexagonal polymorph persists over a narrow temperature range and below 300 K splitting of the *hl*-dominated reflections indicate an increasing orthorhombic distortion, Figure 1d. The projection of these unit cells is shown in the *ab*-plane in Figure 1e and signature reflections in the PND data are shown in Figures 1b-d.

There are several possibilities of space group sequence, and hence structural evolution during this sequence of transitions, (Figure S1a); the exact phase transition sequence on cooling was determined using Rietveld refinement of PND data guided by physical property measurements (full structural details and methodology for structure determination is given in the Supporting Information). The distortion modes associated with the assigned space groups relative to the parent aristotype were visualised and their magnitudes determined using ISODISTORT[33].

The unit cell parameters (reduced to that of the high symmetry $P6/mmm$ aristotype) are shown in Figure 2a; these parameters are insensitive to the exact space group assigned but are a useful aid in corroboration of the assigned structural changes. A phase-matchable second harmonic generation (SHG) signal $280\times$ that of α-quartz (Figure S1b) indicates that $CsNbW_2O_9$ is non-centrosymmetric at room temperature and, in combination with the clear in-plane unit cell tripling, this aids symmetry assignment of a non-polar to polar ($P6/mmm \rightarrow P6mm$) transition at $T_C \sim 1100$ K. The cell tripling is associated with an antiferrodistortive K_3 mode (zone boundary at $q = 1/3, 1/3, 0$) which describes alternating "two-up, one down" displacements of the B-cations along the c-axis. Although the dominant K_3 mode is non-polar, refinements and SHG data indicate that it couples to a secondary polar Γ_2^- mode (zone centre); this coupling of non-polar and polar modes and non-maximal group-subgroup relationship between the polar and non-polar space groups (i.e. cell tripling in this case) is the signature for improper ferroelectricity – this raises the intriguing possibility of a complex domain structure with a high probability of charged domain walls, as discussed later. Dielectric data obtained at 1 MHz indicate a peak in the relative permittivity at this temperature, Figure 2b, consistent with the improper ferroelectric T_C of 1100 K; dielectric losses are high, due to the onset of significant dc conductivity and electrode polarisation. Also, the expansion of the c-axis, on cooling, as T_C is approached is consistent with the alternate two-up, one-down B-cation displacements (the multiplicity is 2:1 for the B1 and B2 sites). It is important to note that no evidence for B-cation ordering is observed during refinements of the PND data at any temperature, with site occupancies indicating that the Nb^{5+}/W^{6+} cations are randomly distributed across the B-sites.

The c-axis doubling peak observed below 350 K is associated with 'rigid' octahedral tilting; this transition into space group $P6_3cm$ is associated with an A_3^+ mode (identified by Whittle *et al.* as the most common tilt configuration in HTBs due to the octahedral connectivity[34]) and results in a similar 'all-in, all-out' tilting of octahedral "trimers" similar to the hexagonal manganites. The onset of tilting is also clearly manifested in a collapse of the c-axis, Figure 2a. On further cooling to below ambient there is an orthorhombic distortion described by an A_6^+ mode (tilting and distortion of the octahedra) and an associated transition to space group $Cmc2_1$ with $a \approx 22.1$ Å ($3a_{HTB}$), $b \approx 12.8$ Å ($\sqrt{3}a_{HTB}$) and $c \approx 7.9$ Å ($2c_{HTB}$). The degree of orthorhombic distortion is relatively small (0.034% orthorhombic strain at 73 K) as denoted by the small divergence in a and b parameters. The overall phase transition sequence is therefore:

$$Cmc2_1 \underset{\sim300\ \text{K}}{\rightleftharpoons} P6_3cm \underset{\sim355\ \text{K}}{\rightleftharpoons} P6mm \underset{\sim1100\ \text{K}}{\rightleftharpoons} P6/mmm$$

A summary of the unit cell metrics for each space group is given in caption for Figure 2 and Table S1. The phase transitions are indicated as dashed lines in Figures 2a-d. The magnitudes of the relevant distortion modes associated with each structure are shown as a function of temperature in Figures 2c-d and clearly show the evolution of the structure from the viewpoint of the individual distortions described above. Regions where distortion mode amplitudes must be zero are included for completeness.

Structurally, the important result of the improper ferroelectric transition is that the displacive K_3 mode is dominant and generates rings of B-cation octahedra (which create the Cs-containing hexagonal channels) formed EITHER only by octahedra in which the cations are displaced in an alternate up-down configuration (*i.e.* alternating B1 and B2 octahedra) OR are all displaced in the same direction (B1 octahedra only), Figure 2e. In the latter, the displacement direction coincides with the that of the Γ_2^- mode and hence net polarization, and therefore gives a proxy for visually determining $\pm P$. The *c*-axis net polarisation, P_Z, was calculated using a point charge model[35] and gives a value of *ca.* 12 μCcm^{-2} at room temperature (Figure S9).

Although the modes involved in symmetry breaking at T_C are the same as those in YMnO$_3$ the underlying mechanism is significantly different. In YMnO$_3$ the K_3 mode describes 'two-up, one-down' Y^{3+} displacements which are correlated with tilting of the MnO$_5$ trigonal bipyramids; the so-called 'trimerisation'. In YMnO$_3$ (and the other rare earth manganites) this 'all-in, all-out' trimerisation is a geometrically driven effect dependent on the A-cation size. In contrast, the non-polar K_3 mode in CsNbW$_2$O$_9$ contains no tilting component and involves only cation displacements in the *c*-axis; the purely displacive nature indicates it is therefore electronically driven by a second order Jahn-Teller (SOJT) effect rather than a geometric (size driven) mechanism.

As d^0 cations, both W^{6+} and Nb^{5+} are well known 'distorters' prone to off-centring[36] due to the SOJT effect whereby the empty *d* orbitals hybridise with the filled oxygen 2*p* orbitals. The extent of the orbital mixing is dependent on the energy gap between the *d* and 2*p* orbitals. Neither CsTaW$_2$O$_9$ (Figure S5), nor Cs$_{0.33}$WO$_3$ (CsW^{5+}W$^{6+}_2$O$_9$)[37] display cell tripling, consistent with the higher energy of the 5*d* orbitals for Ta and W relative to the Nb 4*d* orbitals, and reduced SOJT effect. This clearly suggests that the cell tripling K_3 mode is

triggered by the presence of Nb^{5+} at the B-site. This electronically driven mechanism of symmetry-breaking could have important implications for the developing domain microstructure at T_C in contrast to the geometrically driven origin in the RMnO$_3$ manganites. In the latter, domain density has been shown to be highly dependent both on the R-cation and also the rate at which the material is cooled through T_C[38]. The electronic SOJT effect in CsNbW$_2$O$_9$ is a local effect and should therefore be very susceptible to B-site doping with non-SOJT active cations which could disrupt the important K_3 mode. This is supported by the observation that on partial replacement of Nb with Ta the superlattice peak associated with the cell tripling broadens (Figure S5), which is also consistent with destabilisation of the B-site displacements and a decrease in density of antiphase boundaries. The other obvious difference between CsNbW$_2$O$_9$ and $e.g.$ YMnO$_3$ is that the latter is also an (A-type) antiferromagnetically ordered multiferroic below $T_N \approx 70$ K, whereas there are no magnetically active ions present in CsNbW$_2$O$_9$. However, it is also important to point out that magnetic ordering in the manganites is not important for their DW functionality.

Much of the interest in the hexagonal manganites, which also display this combined K_3 plus Γ_2^- mode symmetry breaking, focusses on their distinctive topologically-protected 'cloverleaf' domain structure, and it is natural to consider analogous behaviour in CsNbW$_2$O$_9$. Formation of the six-domain vertices and topology of the domain walls in the manganites have been studied extensively and are known to originate from the six possible domain states, $\alpha^\pm$, $\beta^\pm$, $\gamma^\pm$. These are generated by combination of the three possible translational domains (α, β, γ) associated with cell tripling (K_3 mode), and the two possible polarization directions (orientational domains), $+P$ and $-P$, associated with the Γ_2^- mode.[21, 26, 39] Choi $et\ al.$[21] analysed the topology of the domain boundaries and proposed an interlocking of antiphase and ferroelectric boundaries such that these combine to form topological defects at the junction of the six domains (these have been commonly referred to these as vortices/antivortices depending on the degenerate winding order of the observed order parameter: vortex - α^+, β^-, γ^+, α^-, β^+, γ^- or antivortex - α^+, γ^-, β^+, α^-, γ^+ β^-; however, this is somewhat misleading as the order parameter does not 'rotate' around the vertex and associated winding numbers have little meaning). An alternative origin proposed for the six-domain cloverleaf involves the presence of both interlocked translational-orientational domain boundaries and orientational-only boundaries, $e.g.$ α^+, α^-, β^+, β^-, γ^-, γ^+; however this possibility was discounted by Jungk $et\ al.$ who demonstrated that all boundaries respond to an applied field[39]. This is also supported by Landau theory[25] and density functional theory

(DFT) calculations[40] which show that combined translational-orientational boundaries with change of phase ($\Delta\Phi = \pi/3$) are of lower energy than orientational-only boundaries ($\Delta\Phi = \pi$).

Following the methodology of Choi *et al.*[21] we can identify two types of antiphase boundaries in $CsNbW_2O_9$, APB_I and APB_{II}, at the junction of the translational domains, and a ferroelectric boundary, FEB, between orientational domains, Figures 3a-c. Note again, in contrast to the trimerisation of MnO_5 polyhedral tilting as a frame of reference for $YMnO_3$, the purely displacive nature of $CsNbW_2O_9$ means that B1-cation displacements are used in this case; these are represented by solid pink and dashed green hexagonal channels formed by octahedra with B1 displaced either all up or all down and which indicate P^+ and P^-, respectively. Both APB_I and APB_{II} cause significant disruption of the cation displacements around the hexagonal channels, but in the FEB the atoms at the boundary are centred to relieve strain. If the APB and FEBs interlock in a similar manner to $RMnO_3$ the result is the same six-domain vertex, Figures 3d,e.

The predicted domain microstructure of $CsNbW_2O_9$ was investigated via transmission electron microscopy (TEM). There are two main mechanisms by which ferroelectrics can give contrast in TEM. Firstly, many proper ferroelectrics are also ferroelastic and there is a large coupled distortion of the unit cell, which results in crystal tilts at each domain boundary. This means large changes in contrast as the diffraction condition is different in the domains either side of the boundary. $CsNbW_2O_9$ is an improper ferroelectric and does not have a ferroelastic distortion, so this mechanism is not applicable. In this case, the second, and weaker source of image contrast from ferroelectrics in TEM is the only possibility. Friedel's law is not observed for a non-centrosymmetric crystal in which dynamical diffraction occurs, meaning that the intensities of two opposing reflections, when viewed exactly along a zone axis or crystal plane, are not equal: $I(g) \neq I(-g)$. This means that the domain structure can be observed in a dark field imaging mode using a suitable reflection with at least a component along the polarisation direction, $\vec{g}.\vec{P} > 0$[41, 42]. This has been used in previous studies of 180° domains in proper ferroelectrics, where there is also no crystal tilt[42, 43]. Figure 4a shows a dark field image obtained using the $1\bar{5}42$ reflection whilst orientated in a two-beam condition close to the $[0\bar{2}2\bar{9}]$ zone axis, with the corresponding diffraction pattern shown in Figure 4b. This is expected to work as the polarisation direction should be $\pm[0001]$. This is in agreement with the obtained PFM data (discussed below), with the six-domain 'clover-leaf' vertex and meandering domain structure of dark and light

domains clearly visible. This clearly confirms that this material supports a similar domain configuration to that observed in the rare-earth manganites[21]. No domain contrast was observed using the $\pm 2\overline{1}10$ reflections, which is expected as $\vec{g}.\vec{P} = 0$. It is important to re-emphasise that although $CsNbW_2O_9$ undergoes a tilt transition (into the $P6_3cm$ phase) these 'all-in, all-out' octahedral tilts, Figure 2d, do not play any role in the generation of the domain vertices: the symmetry-breaking sequence is purely displacive, *i.e.* electronically driven.

The ferroelectric domain patterns in $CsNbW_2O_9$ were also investigated using piezoresponse force microscopy (PFM). The meandering domain and domain wall microstructures, illustrated in Figures 5 a-c, reflect exactly the TEM observations and obviously closely mimic those normally characteristic of the hexagonal rare-earth manganites ($RMnO_3$). Clear six-domain wall junctions (Figures 5 c,d) are evident and are extremely reminiscent of the signature 'clover-leaf' structures seen in the manganites, where all six allowed domain variants meet (Figure 5d). The meandering nature of the domain walls, coupled with the uniaxial polarisation in the system, guarantees that sections of the domain walls will support polarisation discontinuities. In many of the rare-earth manganites, such discontinuities have been associated with enhanced conductivity measured both through conducting atomic force microscopy (cAFM)[13-15, 44] and localised Hall Effect[16, 45] measurements. Initial investigations using cAFM did not reveal enhanced conduction at domain walls in $CsNbW_2O_9$, but it is unclear that a percolative pathway from the conducting AFM tip to the electrical earth at the base of the ceramic sample had been established. Further characterisation of electroded single grains is therefore required before definitive statements on domain wall conduction in this system can be made.

In summary, we present a new improper ferroelectric, $CsNbW_2O_9$, which exhibits very similar domain microstructures to those already widely-studied in the hexagonal rare earth manganites. $CsNbW_2O_9$, however, differs in two important respects: 1) the system adopts an entirely different crystal structure (that of hexagonal tungsten bronze) and 2) the mechanism of improper symmetry-breaking is purely electronically driven (in contrast to the geometrically driven mechanism in the manganites). This material offers the exciting prospect of a new class of improper ferroelectric materials where complex charged domain wall patterns exist and where an associated richness in domain wall functionality could arise.

Experimental Methods

Sample Synthesis. Polycrystalline $CsNbW_2O_9$ samples were prepared by grinding together caesium nitrate (ALFA 98.8%), niobium (V) oxide (Aldrich 99.9%) and tungsten (VI) oxide (ALFA 98.8%) under acetone. The mixture was pressed into a pellet and heated to 873 K at 15 $Kmin^{-1}$ for 1 h before heating to 1323 K at 15 $Kmin^{-1}$ and holding the temperature for 3 h. The samples were cooled to room temperature at 15 $Kmin^{-1}$. Pellets (*ca.* 10 mm diameter and 1mm thick) for electrical and PFM measurements were pressed under 30,000 psi using an isostatic oil press and sintered at 1383 K for 1 h. After polishing using fine-grained SiC paper (P800) sputtered platinum electrodes capped with cured silver conductive paste cured to provide protection at high temperature were applied on the opposing pellet faces.

Structural Characterisation. Laboratory PXRD measurements were made using a Panalytical Empyrean diffractometer (Cu $K_{\alpha 1}$ radiation). Powder neutron diffraction (PND) was carried out at the ISIS spallation neutron source (Rutherford Appleton Laboratory, UK) on the high-resolution powder diffractometer (HRPD) using the time-of-flight method. Data were collected from 73 K to 1323 K with scans recorded for between 40 and 160 µAh integrated proton current to the target (approximately between one and four hours of continuous beam). Powdered samples (approximately 10 g) were mounted into cylindrical vanadium cans and hermetically sealed for data collection above 473 K, sub-ambient data collection used cans of slab geometry comprised of an aluminium alloy body with vanadium windows. All Rietveld refinements were carried out using the General Structure Analysis System (GSAS) software package; details are provided in the Supporting Information.

Dielectric data were collected at intervals of 1 K with heating/cooling rates of 2 $Kmin^{-1}$ using a Wayne Kerr 6500B impedance analyser. Data were collected over the frequency range of 20 Hz to 10 MHz with an *ac* amplitude of 500 mV.

Electron Microscopy Specimens for TEM were prepared using a Helios Xenon Plasma Focused Ion Beam (FIB), using a FIB lift-out and thinning procedure adapted for use on this instrument, similar to that described by MacLaren *et al.*[46]. TEM images were obtained on a FEI Tecnai T20 microscope operating at 200kV, using conventional diffraction contrast imaging and selected area diffraction. All diffraction data is indexed using the $P6_3cm$ cell.

Piezoresponse force microscopy (PFM). PFM amplitude and phase maps in Figures 5a & b respectively, were acquired using a Veeco Dimension 3100 AFM system with a Nanoscope IIIa controller. Figure 5c is an amalgamation of PFM amplitude and phase maps acquired

using the same AFM system. An EG&G 7256 lock-in amplifier was used to apply an AC bias of 5VRMS with a frequency of 20 kHz to the base of the sample, which had two polished faces. The polished bottom face was electrically contacted using a silver paste electrode, whilst the top face was probed during PFM measurements. Commercially obtained platinum/iridium coated silicon probes, model PPP-EFM, were provided by Nanosensors and used for all PFM measurements presented in Figure 5.

Author contributions
FDM conceived and oversaw the study. JAM collected and analysed the diffraction data with input from ASG, PL and FDM. Electrical data was collected and analysed by JAM under the supervision of FDM. Second harmonic generation, transmission electron microscopy and piezoresponse force microscopy measurements and analyses were carried out by TTT/PSH, SJM/IM, and FJYL/PWT/JMG, respectively. All authors contributed to the writing of the manuscript.

Additional information
The authors declare no competing financial interests. Supporting Information is available from the Wiley Online Library or from the author.
The research data (and/or materials) supporting this publication can be accessed at DOI: 10.17630/af50e959-53a9-4c32-948d-ac36b26ff1cb.

References

[1]   H. Y. Hwang, Y. Iwasa, M. Kawasaki, B. Keimer, N. Nagaosa, Y. Tokura, Nat Mater 2012, 11, 103.
[2]   A. Ohtomo, H. Y. Hwang, Nature 2004, 427, 423.
[3]   A. Aird, E. K. H. Salje, Journal of Physics-Condensed Matter 1998, 10, L377.
[4]   G. Catalan, J. Seidel, R. Ramesh, J. F. Scott, Reviews of Modern Physics 2012, 84, 119.
[5]   J. Seidel, L. W. Martin, Q. He, Q. Zhan, Y. H. Chu, A. Rother, M. E. Hawkridge, P. Maksymovych, P. Yu, M. Gajek, N. Balke, S. V. Kalinin, S. Gemming, F. Wang, G. Catalan, J. F. Scott, N. A. Spaldin, J. Orenstein, R. Ramesh, Nat Mater 2009, 8, 229.

[6]   P. Sharma, Q. Zhang, D. Sando, C. H. Lei, Y. Liu, J. Li, V. Nagarajan, J. Seidel, Sci Adv 2017, 3, e1700512; J. Jiang, Z. L. Bai, Z. H. Chen, L. He, D. W. Zhang, Q. H. Zhang, J. A. Shi, M. H. Park, J. F. Scott, C. S. Hwang, A. Q. Jiang, Nat Mater 2018, 17, 49.

[7]   T. Sluka, A. K. Tagantsev, P. Bednyakov, N. Setter, Nat Commun 2013, 4, 1808.

[8]   G. Sanchez-Santolino, J. Tornos, D. Hernandez-Martin, J. I. Beltran, C. Munuera, M. Cabero, A. Perez-Munoz, J. Ricote, F. Mompean, M. Garcia-Hernandez, Z. Sefrioui, C. Leon, S. J. Pennycook, M. C. Munoz, M. Varela, J. Santamaria, Nat Nanotechnol 2017, 12, 655.

[9]   M. Schröder, A. Haußmann, A. Thiessen, E. Soergel, T. Woike, L. M. Eng, Advanced Functional Materials 2012, 22, 3936.

[10]   A. Tselev, P. Yu, Y. Cao, L. R. Dedon, L. W. Martin, S. V. Kalinin, P. Maksymovych, Nat Commun 2016, 7, 11630; J. Guyonnet, I. Gaponenko, S. Gariglio, P. Paruch, Adv Mater 2011, 23, 5377.

[11]   J. R. Whyte, J. M. Gregg, Nat Commun 2015, 6, 7361.

[12]   R. G. P. McQuaid, M. P. Campbell, R. W. Whatmore, A. Kumar, J. M. Gregg, Nat Commun 2017, 8, 15105.

[13]   D. Meier, J. Seidel, A. Cano, K. Delaney, Y. Kumagai, M. Mostovoy, N. A. Spaldin, R. Ramesh, M. Fiebig, Nat Mater 2012, 11, 284.

[14]   J. A. Mundy, J. Schaab, Y. Kumagai, A. Cano, M. Stengel, I. P. Krug, D. M. Gottlob, H. Dog Anay, M. E. Holtz, R. Held, Z. Yan, E. Bourret, C. M. Schneider, D. G. Schlom, D. A. Muller, R. Ramesh, N. A. Spaldin, D. Meier, Nat Mater 2017, 16, 622.

[15]   J. Schaab, S. H. Skjaervo, S. Krohns, X. Dai, M. E. Holtz, A. Cano, M. Lilienblum, Z. Yan, E. Bourret, D. A. Muller, M. Fiebig, S. M. Selbach, D. Meier, Nat Nanotechnol 2018, 13, 1028.

[16]   P. W. Turner, J. P. V. McConville, S. J. McCartan, M. H. Campbell, J. Schaab, R. G. P. McQuaid, A. Kumar, J. M. Gregg, Nano Lett 2018, 18, 6381.

[17]   W. Wu, Y. Horibe, N. Lee, S. W. Cheong, J. R. Guest, Phys Rev Lett 2012, 108, 077203.

[18]   D. Meier, J Phys Condens Matter 2015, 27, 463003; P. Schoenherr, K. Shapovalov, J. Schaab, Z. Yan, E. D. Bourret, M. Hentschel, M. Stengel, M. Fiebig, A. Cano, D. Meier, Nano Lett 2019, 19, 1659.

[19]   A. P. Levanyuk, D. G. Sannikov, Soviet Physics Uspekhi 1974, 17, 199.

[20]   Y. Ishibashi, Y. Takagi, Japanese Journal of Applied Physics 1976, 15, 1621.

[21]   T. Choi, Y. Horibe, H. T. Yi, Y. J. Choi, W. Wu, S. W. Cheong, Nat Mater 2010, 9, 253.

[22]   J. M. Kosterlitz, Reviews of Modern Physics 2017, 89, 040501.

[23]   B. B. Van Aken, T. T. Palstra, A. Filippetti, N. A. Spaldin, Nat Mater 2004, 3, 164; C. J. Fennie, K. M. Rabe, Physical Review B 2005, 72, 100103.

[24]   A. S. Gibbs, K. S. Knight, P. Lightfoot, Physical Review B 2011, 83, 094111.

[25]   S. Artyukhin, K. T. Delaney, N. A. Spaldin, M. Mostovoy, Nat Mater 2014, 13, 42.

[26]   D. Meier, M. Lilienblum, P. Becker, L. Bohatý, N. A. Spaldin, R. Ramesh, M. Fiebig, Phase Transitions 2013, 86, 33.

[27]   S. M. Griffin, M. Lilienblum, K. T. Delaney, Y. Kumagai, M. Fiebig, N. A. Spaldin, Physical Review X 2012, 2; S.-Z. Lin, X. Wang, Y. Kamiya, G.-W. Chern, F. Fan, D. Fan, B. Casas, Y. Liu, V. Kiryukhin, W. H. Zurek, C. D. Batista, S.-W. Cheong, Nature Physics 2014, 10, 970.

[28]   R. J. D. Tilley, International Journal of Refractory Metals and Hard Materials 1995, 13, 93.

[29]   A. Magneli, Acta Chemica Scandinavica 1953, 7, 315.

[30]   P. G. Dickens, A. C. Halliwell, D. J. Murphy, M. S. Whittingham, Transactions of the Faraday Society 1971, 67, 794; J. Goodenough, Progress in Solid State Chemistry 1971, 5, 145; M. R. Skokan, W. G. Moulton, R. C. Morris, Physical Review B 1979, 20, 3670.

[31]   V. A. Isupov, Ferroelectrics 1998, 211, 209.

[32]   H. Y. Chang, T. Sivakumar, K. M. Ok, P. S. Halasyamani, Inorg Chem 2008, 47, 8511.

[33]   B. J. Campbell, H. T. Stokes, D. E. Tanner, D. M. Hatch, Journal of Applied Crystallography 2006, 39, 607.

[34]   T. A. Whittle, S. Schmid, C. J. Howard, Acta Crystallogr B Struct Sci Cryst Eng Mater 2015, 71, 342.

[35]   Y. Shimakawa, Y. Kubo, Y. Nakagawa, S. Goto, T. Kamiyama, H. Asano, F. Izumi, Physical Review B 2000, 61, 6559.

[36]   M. Kunz, I. D. Brown, Journal of Solid State Chemistry 1995, 115, 395; K. M. Ok, P. S. Halasyamani, D. Casanova, M. Llunell, P. Alemany, S. Alvarez, Chemistry of Materials 2006, 18, 3176.

[37]   L. Kihlborg, A. Hussain, Materials Research Bulletin 1979, 14, 667; J. Oi, A. Kishimoto, T. Kudo, Journal of Solid State Chemistry 1993, 103, 176; J.-S. Lee, H.-C. Liu, G.-D. Peng, Y. Tseng, Journal of Crystal Growth 2017, 465, 27.

[38]   Q. N. Meier, M. Lilienblum, S. M. Griffin, K. Conder, E. Pomjakushina, Z. Yan, E. Bourret, D. Meier, F. Lichtenberg, E. K. H. Salje, N. A. Spaldin, M. Fiebig, A. Cano, Physical Review X 2017, 7, 041014.

[39]   T. Jungk, Á. Hoffmann, M. Fiebig, E. Soergel, Applied Physics Letters 2010, 97, 012904.

[40]   D. R. Småbråten, Q. N. Meier, S. H. Skjærvø, K. Inzani, D. Meier, S. M. Selbach, Physical Review Materials 2018, 2, 114405.

[41]   F. Fujimoto, Journal of the Physical Society of Japan 1959, 14, 1558.

[42]   M. Tanaka, G. Honjo, Journal of the Physical Society of Japan 1964, 19, 954.

[43]   R. Gevers, H. Blank, S. Amelinckx, physica status solidi (b) 1966, 13, 449.

[44]   T. S. Holstad, D. M. Evans, A. Ruff, D. R. Småbråten, J. Schaab, C. Tzschaschel, Z. Yan, E. Bourret, S. M. Selbach, S. Krohns, D. Meier, Physical Review B 2018, 97, 085143.

[45]   M. P. Campbell, J. P. McConville, R. G. McQuaid, D. Prabhakaran, A. Kumar, J. M. Gregg, Nat Commun 2016, 7, 13764.

[46]   I. MacLaren, M. Nord, C. Jiao, E. Yucelen, Microsc Microanal 2019, 115.
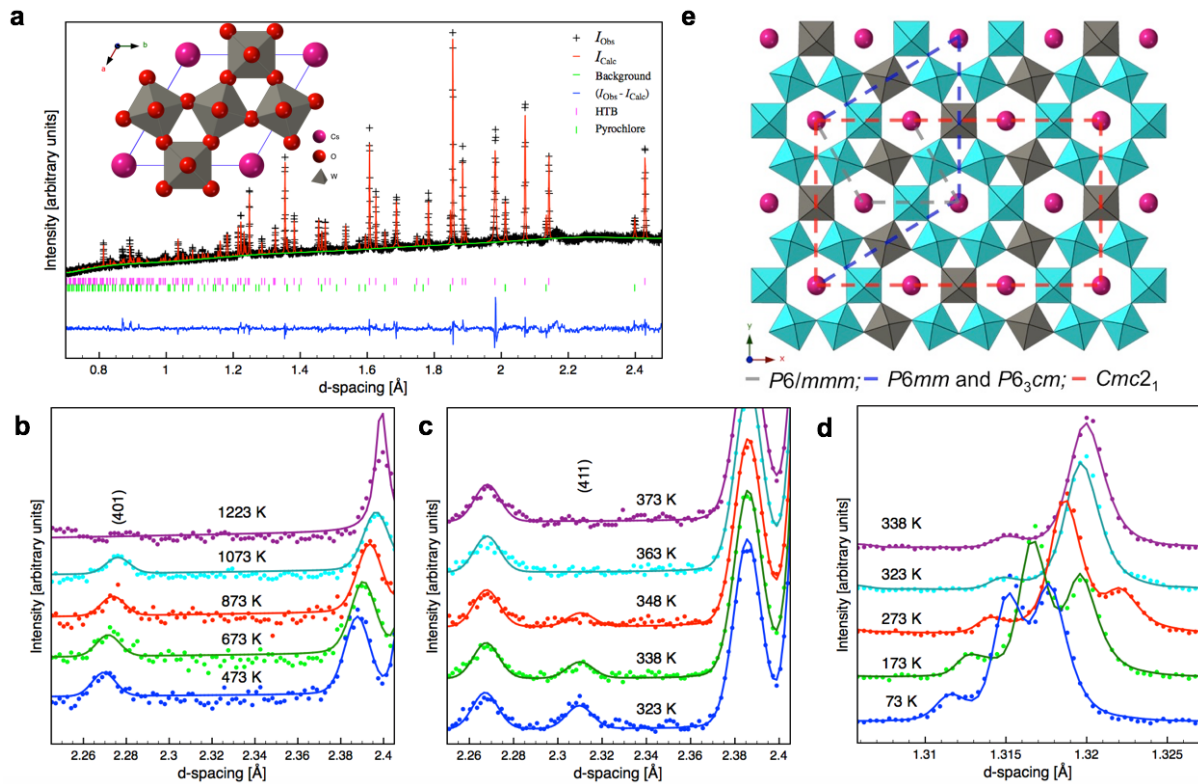
Figure 1 | Structural evolution as a function of temperature. Rietveld refinement profile of powder neutron diffraction data (ISIS HRPD, bank 1) obtained at 1273 K, **a** (see Supporting Information for full refinement details). Upper and lower tick-marks refer to reflections for the high symmetry hexagonal tungsten bronze (HTB) aristotype of $Cs_{0.33}WO_3$ (inset, space group $P6/mmm$) and defect pyrochlore secondary phase, respectively (see main text for details). **b** Evolution of reflections associated with: unit cell tripling in ab plane (reflection (401) in polar space group $P6mm$), **b**; and c-axis doubling ((411) in $P6_3cm$) due to octahedral tilting, **c**. Peak-splitting indicating transition to orthorhombic $Cmc2_1$, **d**. Filled circles in **b-d** represent data points, the solid lines are the Rietveld fits. Polyhedral view of the HTB structure viewed along the c-axis indicating the sequential unit cell expansion in the ab plane on cooling, **e**.
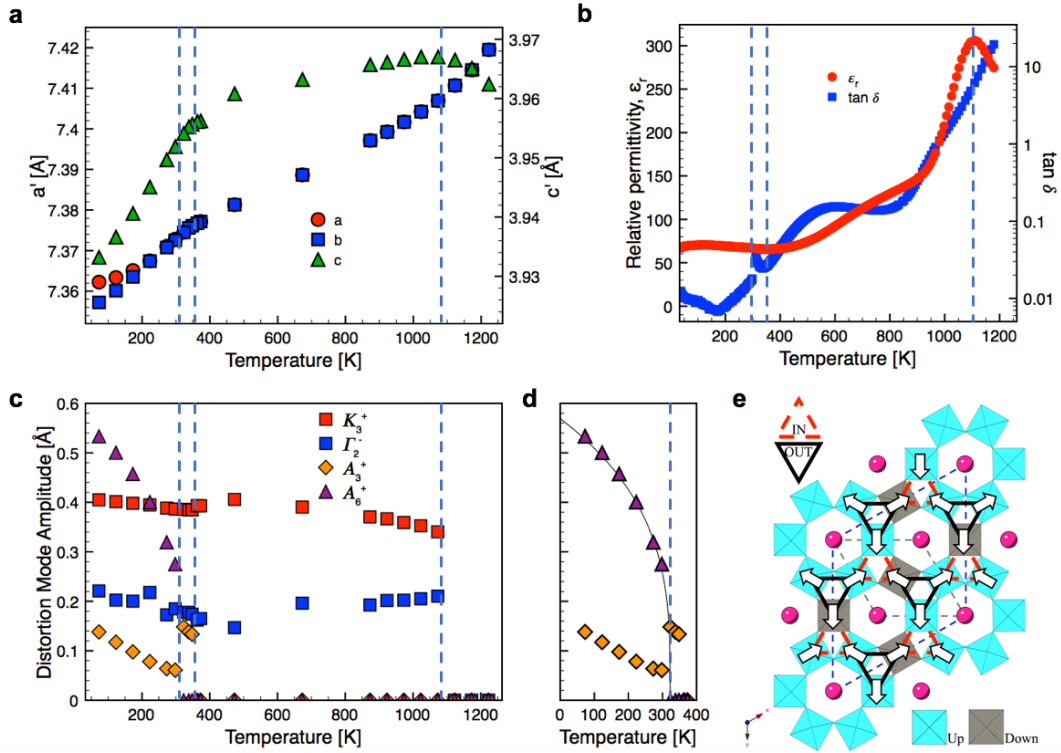
Figure 2 | Onset of improper ferroelectricity. a Unit cell dimensions as a function of temperature consistent with symmetry breaking sequence described in the main text. (Pseudo-hexagonal) cell dimensions have been reduced relative to the $P6/mmm$ aristotype which has $a' = a$ and $c' = c$: $P6mm$ $a' = a/\sqrt{3}$, $c' = c$; $P6_3cm$ $a' = a/\sqrt{3}$, $c' = c/2$; $Cmc2_1$ $a' = a/3$, $a' = b/\sqrt{3}$, $c' = c/2$. **b** Dielectric data (at 1 MHz) as a function of temperature indicating a peak at the Curie point at ca. 1100 K. **c** Irreducible representation (symmetry mode) analysis as a function of temperature indicating improper symmetry breaking at $T_C \sim 1100$ K via coupling of non-polar K_3 (cell tripling) and polar Γ_2^- modes which results in 'two-up, one-down' B-cation displacements and net polarisation, respectively. At lower temperature, this is followed by octahedral tilting in the c-axis (A_3^+) and finally an octahedral distortion (A_6^+) leading to orthorhombicity, **d**. The initial symmetry breaking to the polar phase ($P6mm$) is purely displacive and results in 'hexamerisation' of B-cation displacements around the hexagonal channels where these consist either of alternating "up-down" or "all-up" octahedra, **e**. The secondary effect of tilting at lower temperature results in 'all-in, all-out' octahedral trimers more reminiscent of the rare earth manganites.
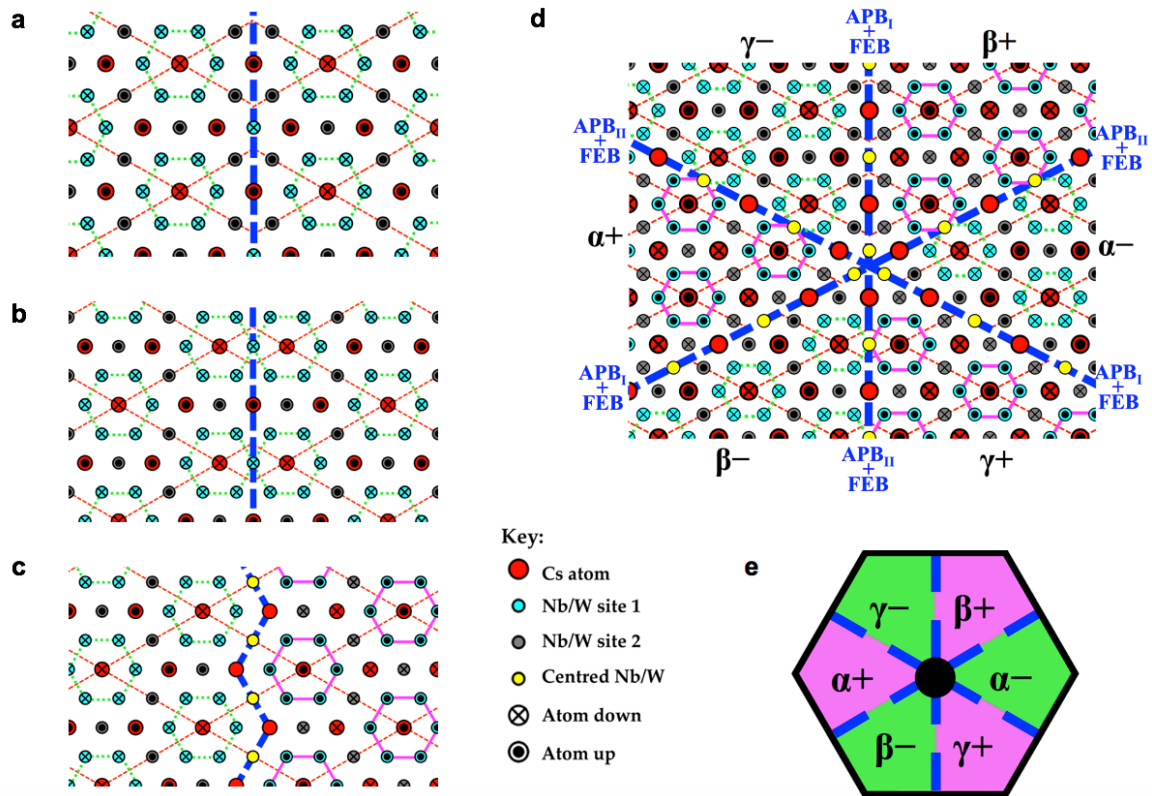
Figure 3 | Structural origins of the expected ferroelectric domain structure in CsNbW₂O₉. Below T_C the three possible translational domain states (α, β, γ) generated during unit cell tripling (K_3 mode) combine to generate two types of antiphase boundaries APB$_I$ and APB$_{II}$, **a, b**. The polar $\varGamma_2^-$ mode generates two possible orientations of polarisation for each translational domain (*i.e.* $\alpha^\pm$, $\beta^\pm$, $\gamma^\pm$) and associated ferroelectric domain boundaries (FEB), **c**. The solid pink and dashed hexagons denote hexagonal channels with B-cation displacements either all-up or all-down (see Figure 2e) and indicate P^+ and P^-, respectively. Interlocking of translational and orientation domains such that both the phase (α, β, γ) and polarisation orientation ($\pm$) changes at domain boundaries by combination of the APB and FEB resulting in a six-state 'cloverleaf' domain configuration, **d, e**, comparable to that observed in YMnO₃. (Following the methodology of Choi *et al.*[21]).
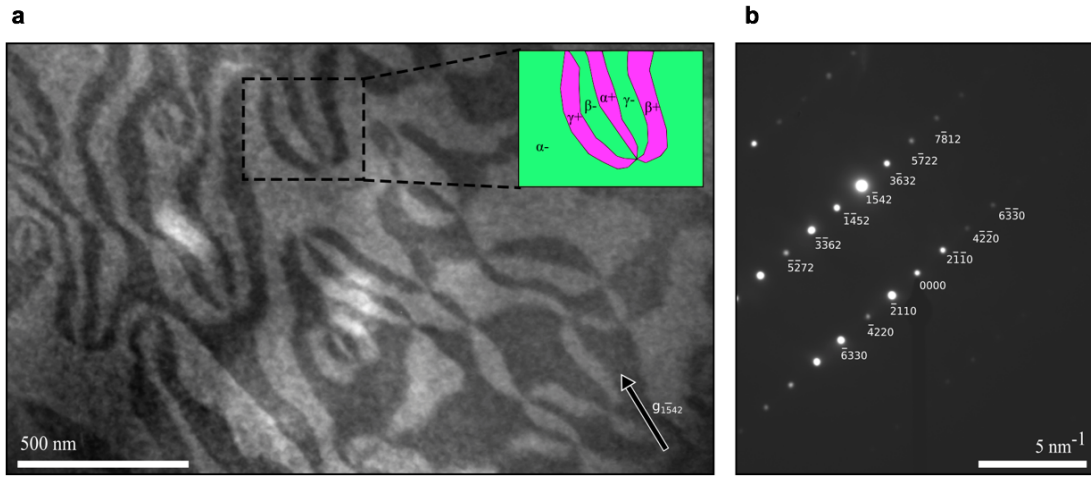
16

Figure 4 | Transmission Electron Microspcopy (TEM) of CsNbW$_2$O$_9$. TEM images recorded along or close to the $[0\bar{2}2\bar{9}]$ direction: dark field image of the domain structure obtained using the $1\bar{5}42$ reflection, **a**, and the corresponding indexed diffraction pattern, **b**. The inset in **a** shows a six-domain vertex and the overlay details its three structural domain variants (α, β and γ) and two polar domain variants (+ and -).
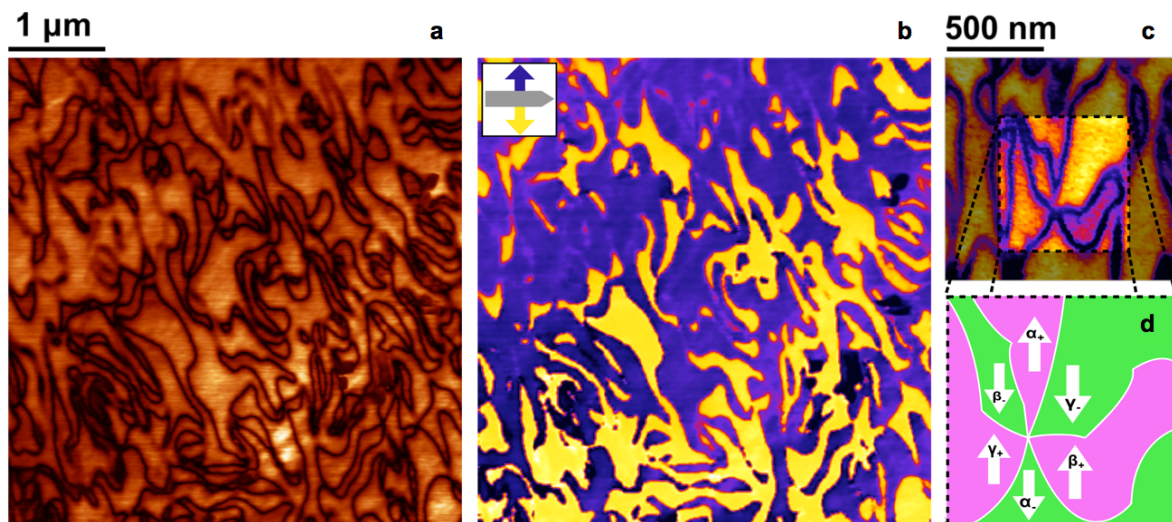
Figure 5 | Piezoresponse Force Microscopy (PFM). Lateral PFM amplitude, **a**, and phase, **b**, maps on a $CsNbW_2O_9$ grain with little out-of-plane piezoactivity; such domain microstructures are extremely reminiscent of those seen in the rare-earth manganites. **c** is a higher resolution domain map showing so-called $Rcos\theta$ data (where PFM amplitude is multiplied by the phase at each point); this map explicitly demonstrates the existence of six-domain junctions, normally characteristic of the hexagonal rare-earth manganites. The cartoon in **d** labels the three structural and two polar domain variants, resulting from the trimerisation parameter emerging during the improper ferroelectric transition.

Table of contents
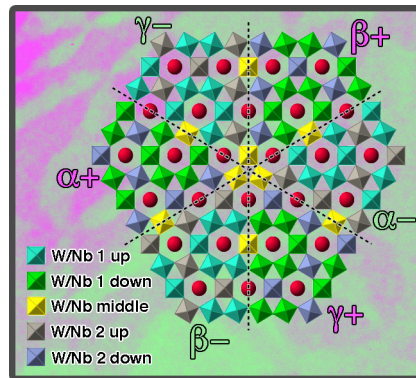
We report a novel electronically driven improper ferroelectric hexagonal tungsten bronze, $CsNbW_2O_9$. This compound displays the same domain microstructure found in the hexagonal manganites, such as characteristic six-domain 'cloverleaf' vertices and domain wall (DW) sections with polar discontinuities. This new material class, with domain patterns already known to generate interesting functionality, is important for the emerging field of DW nanoelectronics.